A new damage identification approach based on impedance-type measurements and 2D error statistics

Costas Providakis[*1], Stavros Tsistrakis[1], Maristella Voutetaki[1], Yiannis Tsompanakis[2], Maria Stavroulaki[1], John Agadakos[1], Eleftherios Kampianakis[1] and George Pentes[1]

[1]*School of Architectural Engineering, Technical University of Crete, GR-73100 Chania, Greece*
[2]*School of Environmental Engineering, Technical University of Crete, GR-73100 Chania, Greece*

Abstract. The electro-mechanical impedance (EMI) technique makes use of surface-bonded lead zirconate titanate (PZT) patches as impedance transducers measuring impedance variations monitored on host structural components. The present experimental work further evaluate an alternative to the conventional EMI technique which performs measurements of the variations in the output voltage of PZT transducers rather than computing electromechanical impedance (or admittance) itself. This paper further evaluates a variant of the EMI approach presented in a previous work of the present authors, suitable, for low-cost concrete structures monitoring applications making use of a credit card-sized Raspberry Pi single board computer as core hardware unit. This monitoring approach is also deployed by introducing a new damage identification index based on the ratio between the area of the 2-D error ellipse of specific probability of EMI-based measurements containment over that of the 2-D error circle of equivalent probability. Experimental results of damages occurring in concrete cubic and beam specimens are investigated under increasing loading conditions. Results illustrate that the proposed technique is an efficient approach for identification and early detection of damage in concrete structures.

Keywords: concrete damage detection; electromechanical impedance; Raspberry PI; PZT sensor/actuator

1. Introduction

Concrete structures have a long service life compared to other mechanical, electrical and electronic commercial products. But, on the other hand, concrete structures age and deteriorate with time due to various factors who adversely affect its safety and structural integrity. As a consequence, the development of damage detection techniques becomes a matter of utmost importance. The movement towards smart structures is one of the most interesting and promising new developments in the field of structural health monitoring (SHM) process of concrete structures. The need for real-time, in-situ damage detection techniques for concrete structures has leaded to develop various successful experimental approaches dedicated to prevent catastrophic failures and to reduce the cost of maintenance and inspecting tasks. One of the most promising experimental techniques is the so called electromechanical impedance (EMI) or its inverse

---

*Corresponding author, Professor, E-mail: cpprov@mred.tuc.gr

admittance (EMA) approach (Park *et al*. 2000, Song *et al*. 2007, Tawie and Lee 2010, 2011, Tseng and Wang 2004, Park *et al*. 2006, Yang *et al*. 2008, Shin and Oh 2009, Yang and Divsholi 2010, Annamdas *et al*. 2010, Park *et al*. 2011, Wang and Zhu 2011, Na and Lee 2012); This approach uses electromechanical impedance (admittance) spectrum signatures acquired across the electrodes of piezoelectric patches which are surface bonded or embedded inside the body of concrete structural components. More specifically, it is based on the direct relation existed between the PZT impedance and structural mechanical impedance which, in turn, is affected by the presence of damage.

During the initial years of EMI development, the research efforts mainly focused on exploring the possible application of EMI technique on various mechanical and structural systems using commercialized equipments, such as the Agilent 4294A or the HP 4192A impedance analyzers, which can cost as much as 40,000 US dollars. Those equipments were commonly used to measure the two desired PZT impedance (or its inverse admittance) parameters: the conductance, which is the real part of impedance, and the susceptance, which is the imaginary part of impedance, for each measurement. However, due to the high cost, such equipment may not always be available to be used for the impedance based structural health monitoring process. To address the issues of prohibitive cost and portability, a PZT active sensing monitoring system has been developed in a previous work of the present authors (Providakis *et al*. 2015) using an approach which basically has the benefits of hardware simplicity but not limited by the data acquisition (DAQ) device sampling rate which is currently required to replace the high cost commercial impedance analyzers (Peairs *et al*. 2004, Na and Lee 2012).

One of the objectives of this paper is to further evaluate the structural health monitoring system of the work of Providakis *et al*. (2015) that uses lead-zirconate-titanate patches (PZT) as sensors and actuators, to detect damage in a concrete structure. This monitoring system includes a wireless telemetry system for measurements storing and retrieving purposes. The basic idea behind this system is to measure the spectrum variations in the peak output voltage response signal, generated across the poles of PZT patches bonded on the surface of the investigated concrete structures. These variations are directly related to the variations of the electromechanical impedance (admittance) spectrum signatures and behave analogously with them in the presence of damage.

From the perspective of the damage identification, Sekhar (2008) provided an extensive review work on research developments in damage identification of civil structural components. It is proved that different parameters could be accompanied with damage but in the same time those parameters may be correlated with other relevant information getting various results with varying accuracy in distinguishing the damage. For this reason, seeking a proper selection or combination of appropriate damage criterion parameters is an imperative purpose. In our case where the measured quantity is the spectrum variation in the PZT peak output voltage response signal, the damage criterion should be a scalar quantity that results from the comparative processing of that response signal. To date, several damage metrics have been proposed to detect damage and used to test the effectiveness of various structural health monitoring systems. Among them, the most popular are (Tseng *et al*. 2001): the root mean square deviation (RMSD), the mean absolute percentage deviation (MAPD), and the correlation coefficient deviation (CCD). Nevertheless, development of a suitable and reliable damage metrics is still an issue to be investigated. In this paper, a new damage identification metric is introduced based on two-dimensional error statistics. When trying to identify structural damage the question arises of "How much close does the measurement of any current structural integrity condition and pristine (healthy) integrity condition have to be in order to achieve a particular confidence limit?" For structural damage identification

purposes a confidence limit of approximately 99.5% is used in the present work. To examine the error variation of a PZT peak output voltage response signal point at a specific frequency between pristine structural condition and any other current structural condition under a particular confidence limit, a two-dimensional error analysis is required. Two dimensional error analyses have been extensively used mainly to depict the accuracy of radiolocation and navigation systems (Mertikas 1985, Chin 1987). The application of this idea in structural damage identification significantly simplifies the process by introducing a new damage metric which, in other words, represents the variation of the covariance matrix for 2D normally distributed spectrum measurement data, according to a chosen confidence value.

The proposed methodology is effectively applied to the damage detection of concrete beam specimens proving that might be considered as an alternative to conventional structural health monitoring techniques.

2. Electro-mechanical impedance (EMI) method

The EMI technique uses piezoelectric materials, such as Lead Zirconate Titanate (PZT), which exhibit the characteristic feature to generate surface charge in response to an applied mechanical stress and conversely, undergo mechanical deformation in response to an applied electric field. Consider a structural component with a PZT patch bonded on it. The related interaction model is shown in Fig. 1 for a square PZT patch of length 2ℓ and thickness h.

Let's say that a sinusoidal voltage signal is generated across PZT electrodes. This signal can be expressed as a function of time in the form

$$V_{pzt}(t) = V_p \sin(\omega t) \tag{1}$$

where V_{pzt} (t) is the voltage across the direction of the axis y_3 at time t, V_p is the peak voltage of the voltage signal and ω is the radial frequency. The relationship between radial frequency ω (in radians/second) and frequency f (Hz) is $\omega = 2\pi f$.

In a linear system, the response current signal I(t) is shifted in phase φ and has a different peak current I_p
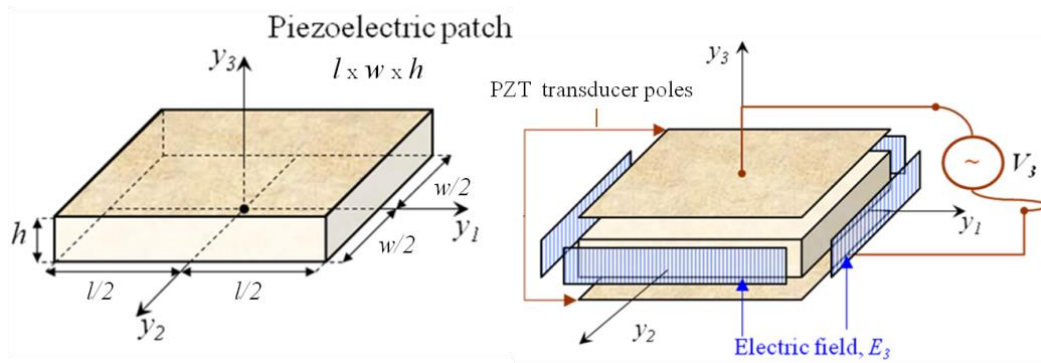
$$I(t) = I_p \sin(\omega t + \varphi) \tag{2}$$

Fig. 1 Interaction model of PZT and concrete structure

Taking into account that every PZT under a pure and high frequency sinusoidal voltage signal behaves almost like a capacitive system which tends to preserve negligible phase difference between voltage and current output signal, the impedance amplitude can be evaluated by

$$|Z(\omega)| = \frac{V_p(\omega)}{I_p(\omega)} \cong \frac{V_p(\omega)}{\frac{V_{in}(\omega)}{|Z(\omega)|+R_f}} \tag{3}$$

Then, the peak value $V_p(\omega)$ of the voltage V_{pzt} across the PZT transducer is estimated by solving the previous equation in terms of $Vp(\omega)$

$$V_p(\omega) \cong \frac{|Z(\omega)|}{|Z(\omega)|+R_f} \cdot V_{in} \tag{4}$$

Based on the above equation, it is obvious that $V_{pzt}(\omega)$ and particularly the peak voltage signal $V_p(\omega)$ provides a solid indication for the value of $|Z|$ being directly dependent on any observed impedance amplitude variations.

In the present work, an innovative structural monitoring system denoted as WiAMS proposed by the present authors in Providakis *et al*. (2015) is further investigated to detect damage in concrete structures. WiAMS is a wireless system for estimating the impedance magnitude $|Z|$ of a PZT device that is utilized for concrete integrity monitoring. Particularly, WiAMS offers extensive features such as remote control, high processing power and wireless data upload to SQL database, email notifications, scheduled, iterative $|Z|$ estimations and frequency span from 5 kHz to 300 kHz resolution down to 1 Hz. WiAMS is consisted of multiple custom-made modules that conduct the $|Z|$ estimation and its prototype is depicted in Fig. 2. Particularly the modules are:
1. A single board computer (SBC) Raspberry Pi.
2. A custom board with the AD7357 ADC.
3. A custom board with the AD9837 frequency generator.
4. A custom interface board responsible for the power supply and the connection of the rest modules between them and with the Raspberry Pi.
5. The PZT driver module.
6.

The core hardware element of WiAMS which has been used as SBC in this work is the second version of Raspberry PI also known as Raspberry Pi model B as shown in Fig. 2. Raspberry PI is the central control unit of WiAMS because it communicates and controls the integrated circuit modules of the system. Also due to its connection to the Internet, enables the user to control the system remotely using a terminal emulator (in the present work, PUTTY free open source application), be informed via mail and sends itself Raspberry pi measurement results for storing reasons to web databases. Due to its small size and weight (Raspberry Pi is credit card-sized) it can be placed on the specimen under test without affecting its dynamic features. Additionally, considering the device's low cost, a number of devices can be used for simultaneous scanning of a large scale structure.

The SBC is used as the coordinator of the system that performs multiple tasks. Particularly the SBC controls the frequency output of the frequency generator and collects the digital data from the ADC, via serial peripheral interface (SPI). The SBC accommodates a powerful ARM processor and its operating system is Linux-based. Therefore it has extended connectivity and calculating capabilities that WiAMS takes advantage of, in order to facilitate remote structural integrity monitoring sending measurements results for storing reasons to web databases as shown in block diagram of Fig. 3.
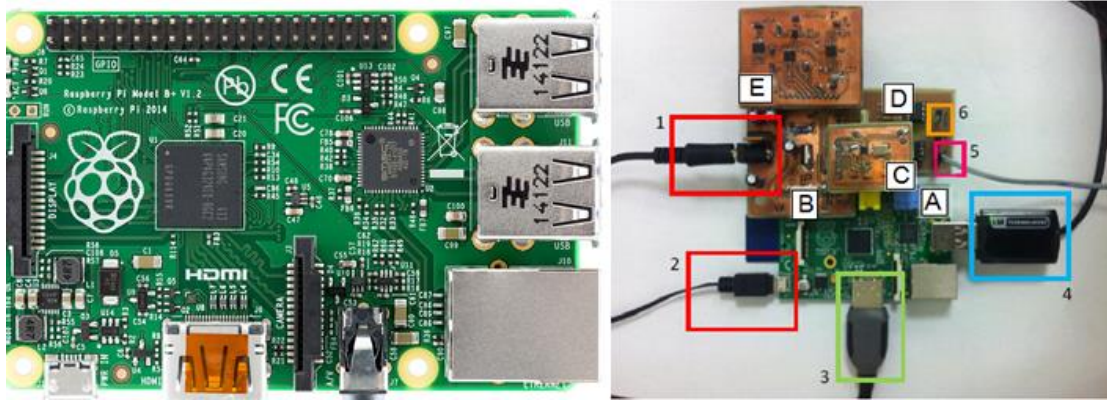
Fig. 2 Raspberry Pi SBC (left), WiAMS Prototype (right)

(1) Power supply, 12 V DC 2.5A   (A) Raspberry Pi
(2) Power supply, 5 V DC 1A   (B) Interface Board
(3) HDMI port for connection with screen (C) Generator Module
(4) Wi-Fi USB   (D) Peak Detector Module
(5) Connection with PZT electrodes   (E) ADC Module
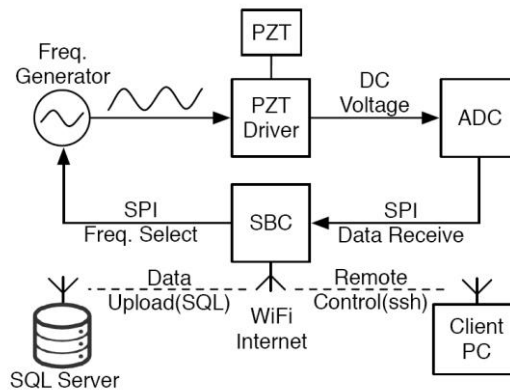(6) Reference resistor

Fig. 3 The WiAMS block diagram

The SoC of the Raspberry P Model B is a Broadcom BCM2835. The SoC contains an ARM11 processor that uses ARMv6 architecture core with floating point running at 700 MHz and Videocore 4 GPU along with 512 MB SDRAM. It has a 10/100 Mbps RJ45 ethernet port alongside two USB 2.0 ports which can also be used for network connectivity by connecting Wi-Fi dongle or USB internet stick to this port. It has a SD card slot for data storage and operating system. An external SD card with operating system configured on FAT32 partition is required that is plugged

in on Raspberry Pi as it does not have onboard storage facility. It is powered through micro-USB port or GPIO pins with 5V DC, 700-1500 mA power supply. It provides scalability port that gives interface and communication capabilities through various protocols (UART, SPI) with other integrated circuits. Also has connectivity to the internet. The operating system that exists in it to operate is a Unix-type OS.

The other modules ADC, DDS, Peak detector are connected for the needs of this work by using a custom made interface board with a block diagram shown in Fig. 4.

2.1 WiAMS modules functionality

As mentioned above, the PZT transducer must be excited by a range of sinusoidal frequencies. This excitation is achieved by the custom-made DDS module which contains the AD9837 function generator to generate predefined sinusoidal frequency ranges appropriate to activate the PZT transducer.

The Peak detector module is directly connected to the PZT transducer and detects its peak voltage response value. More specifically, WiAMS introduces the frequency generated by the DDS module, which is then amplified and applied as a voltage signal $V_{in}(\omega)$ to the PZT transducer. Conversely, the peak voltage response output of the PZT transducer passes through the Peak detector to measure the peak voltage response $V_{pzt}(\omega)$ of the PZT transducer.

Then to digitally measure the PZT peak voltage response a custom-made ADC module is used. The ADC module which contains the AD7357 ADC converts the value of the peak voltage response signal from analog to digital form, by using accuracy of up to 14 bits. Once it is converted, the measured value is transferred to Raspberry pi and stored on it.

The operation software of WiAMS is consisted of the Unix-type Raspberry pi operating system and the custom-made script codes that control the modules of the system. The main modules of the control code are written in C language and a bash shell script language working as in Fig. 5:

The system operates as follows. When the SBC is initialized (boots-up) it automatically connects to internet via a WiFi USB dongle. Following, the IP address and the Raspberry Pi serial number are sent via email to a preprogrammed email address. The user can connect to the SBC and have full control over it with a simple secure-shell (ssh) client such as Putty.
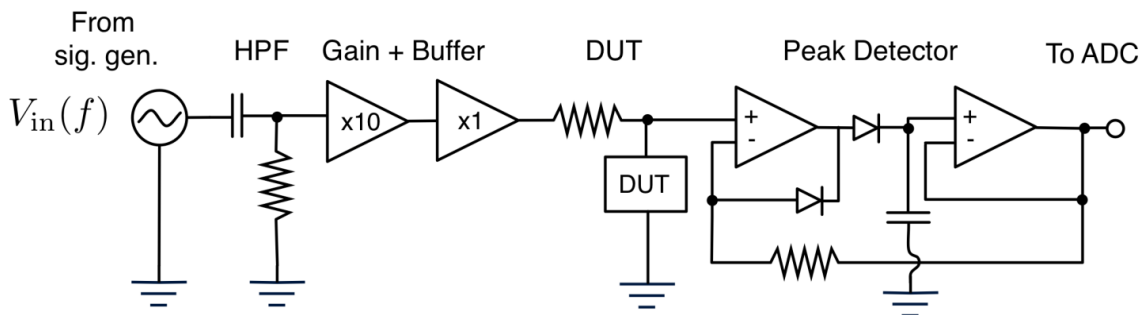

Fig. 4 Interface block diagram

The user can select: either to be informed via mail, for the database on which the measurements are saved, for the initial and final frequency of the spectrum, for the frequency scanning step, for how many times you may repeat the measurement and for how long. The system is also enriched by an ability to run sets of synchronous measurements taken at specific times.

Finally the end-user can retrieve the measurement values either as obtained directly by the WiAMS command system, or by the connected Internet database or through the email received by the user or even through the Raspberry Pi itself by loading the stored file of the measurement results.

3. Damage index based on 2D elliptical and circular error statistics

Let assume that the peak output voltage response signal measurements for the healthy baseline structural condition at any predefined frequency range ω_i (i=1,..No) is denoted by X while for any other different from healthy baseline structural condition, the peak output voltage response signal measurements at the same frequencies is denoted by Y. Let also assume that the pair X and Y may be considered as random normal, or Gaussian, variables which can be expressed in vector form as in the works of Mertikas (1985) and Chin (1987)

$$Z = \begin{bmatrix} X \\ Y \end{bmatrix} \tag{5}$$

The mean of this Gaussian random vector is defined as

$$E[Z] = E \begin{bmatrix} X \\ Y \end{bmatrix} = \begin{bmatrix} m_X \\ m_Y \end{bmatrix} \tag{6}$$

while the covariance matrix of this vector can be defined as

$$\Sigma = \begin{bmatrix} \sigma_X^2 & \sigma_{XY} \\ \sigma_{XY} & \sigma_Y^2 \end{bmatrix} \tag{7}$$

where $\sigma_X{}^2$ and $\sigma_Y{}^2$ are the variances of the random variables X and Y and σ_{XY} is the covariance of X and Y. Then, the correlation coefficient of the variables X and Y should be written as

$$\rho = \frac{\sigma_{XY}}{\sigma_X \sigma_Y} \tag{8}$$

According to the previous definitions, the covariance matrix can be rewritten as

$$\Sigma = \begin{bmatrix} \sigma_X^2 & \rho \sigma_X \sigma_Y \\ \rho \sigma_X \sigma_Y & \sigma_Y^2 \end{bmatrix} \tag{9}$$

For this second-order case, the Gaussian PDF particularizes as, with $z=[x\ y]^T$,

$$f(z) = \frac{1}{2\pi\sqrt{det\Sigma}} exp\left[-\frac{1}{2}[x - m_X \cdot y - m_Y]\Sigma^{-1}[x - m_X \cdot y - m_Y]^T \right]$$

$$= \frac{1}{2\pi\sigma_X\sigma_Y\sqrt{1-\rho^2}} exp\left[-\frac{1}{2(1-\rho^2)} \left(\frac{(x-m_X)^2}{\sigma_X^2} - \frac{2\rho(x-m_X)(y-m_Y)}{\sigma_X\sigma_Y} + \frac{(y-m_Y)^2}{\sigma_Y^2} \right) \right] \tag{10}$$

The locus (x, y) for which the PDF is greater or equal to a specified constant K_1 is given by

$$\left\{(x,y): \frac{1}{2\pi\sqrt{det\Sigma}} exp\left[-\frac{1}{2}[x-m_X \cdot y - m_Y]\Sigma^{-1}[x-m_X \cdot y - m_Y]^T\right] \geq K_1\right\} \quad (11)$$

Eq. (11) represent all pairs (x, y) for which the PDF is less or equal to a given specified constant K_1. The locus of constant value is an ellipse which is named ***error ellipse*** with its axis parallel to the x and y coordinates when $\rho=0$, i.e., when the random variables X and Y are uncorrelated while when $\rho\neq0$ the error ellipse axis are not parallel with the x and y axis. The center of the ellipse coincides in all cases with (m_X, m_Y). The length of the ellipses axis and the angle they do with the axis x and y are a function of the constant K_1, of the eigenvalues λ_1 and λ_2 of the covariance matrix Σ and of the correlation coefficient. The eigenvalues of the covariance matrix Σ are given by

$$\lambda_1 = \frac{1}{2}\left[\sigma_X^2 + \sigma_Y^2 + \sqrt{(\sigma_X^2 - \sigma_Y^2)^2 + 4\sigma_X^2\sigma_Y^2\rho}\right] \quad (12a)$$

$$\lambda_2 = \frac{1}{2}\left[\sigma_X^2 + \sigma_Y^2 - \sqrt{(\sigma_X^2 - \sigma_Y^2)^2 + 4\sigma_X^2\sigma_Y^2\rho}\right] \quad (12b)$$

When $\rho=0$, i.e., the variables X and Y are uncorrelated, the locus in Eq. (11) may be written as

$$\left\{(x,y): \frac{(x-m_X)^2}{\sigma_X^2} + \frac{(y-m_y)^2}{\sigma_Y^2} \leq K\right\} \quad (13)$$

with $K = -2\ln(2\pi K_1\sqrt{det\Sigma}$. In this case the error ellipse have axis aligned with the coordinate frame having semi-major x-axis with length $2\sigma_X\sqrt{K}$ and semi-minor y-axis with length $2\sigma_Y\sqrt{K}$. But in case of non-diagonal matrix with $\rho\neq0$ the error ellipse has its axis not aligned with the coordinate frame.

With no loss of generality, lets investigate the simple case of $\rho\neq0$ and $m_X=m_Y=0$, i.e., the error ellipse is centered in the coordinated frame. In this case the coordinate system (x,y) is transformed to a new coordinate system axis w_1, w_2

$$\left\{(w_1,w_2): [w_1 \ w_2]\begin{bmatrix}\lambda_1 & 0 \\ 0 & \lambda_2\end{bmatrix}^{-1}\begin{bmatrix}w_1 \\ w_2\end{bmatrix} \leq K\right\} \quad (14)$$

that corresponds to a rotation of the coordinate system (x, y) around its origin by an angle

$$a = \frac{1}{2}\tan^{-1}\left(\frac{2\rho\sigma_X\sigma_Y}{\sigma_X^2-\sigma_Y^2}\right), -\frac{\pi}{4} \leq a \leq \frac{\pi}{4}, \ \sigma_X \neq \sigma_Y \quad (15)$$

Evaluating (14) yields to an error ellipse having semi-major w1-axis with length $2\sqrt{K\lambda_1}$ and semi-minor w2-axis with length $2\sqrt{K\lambda_2}$. For all the above cases in the special situation of equal eigenvalues, i.e., $\lambda_1=\lambda_2$ we conclude to the case of ***error circle***. with radius $R = K_r\sigma_x$ with K_r being a factor given in terms of ellipticity parameter $c=\sigma_Y/\sigma_X$ as in Chin (1987).
For our damage condition decision making purposes, and given m_X, m_Y and Σ, it is necessary to determine the probability that a given vector of (x, y) pairs will lie within a specific error ellipse given by Equation 11. For a given K the relationship between K and the probability of lying within error ellipse specified by K is

$$\Pr\{probability \ for \ a \ point \ x \ inside \ the \ ellipsoid\} = 1 - e^{-K/2} \quad (16)$$

The value of the area ratio between the area of the error ellipse to the area of the error circle of

the same probability is denoted here as ECAR (Ellipse-to-Circle-Area-Ratio) having the following general form

$$ECAR = \frac{Area\ of\ a\ confidence\ ellipse\ of\ a\ given\ probability}{Area\ of\ the\ confidence\ circle\ for\ the\ same\ probability\ and\ confidence\ level} \qquad (17)$$

To discuss about the efficiency of this index, let's suppose the special case where the probability of error circle and ellipse is 50% (Pr=0.5). For this special case the area of the error circle is (Chin 1987)

$$\pi(R50)^2 = \pi K_r^2 \sigma_x^2 \qquad (18)$$

where R50 is the radius of the error circle, centered in the coordinate frame, that encompasses 50 percent of measurements. The area of the confidence ellipse with a probability of same 50 percent is given as

$$\pi AB = \pi K \sigma_y K \sigma_x = \pi \sigma_x^2 c K^2 \qquad (19)$$

Where K is given as tabulated values in Chen (1987) in terms of probability level (for 50% probability K=1.17742) and A and B are the radius of the semi-minor and semi-major radius, respectively, of the error ellipse, centered also at the coordinate frame, that contains the 50 percent of the measurements. $ECAR_{50}$ index, for this special case of 50% probability, is given by combining Eqs. (17)-(19)

$$ECAR_{50} = (ck)^2 / K^2 \qquad (20)$$

When c is equal to 1 the confidence ellipse becomes the confidence circle of the same probability while when c=0 the confidence ellipse degenerates into a line (linear degeneracy). Taking this interesting conclusion into account, we introduce a new damage index based on the above specified ECAR index for a specific probability as confidence level, i.e., let's say 99.5%. ECAR index has the benefit that could directly characterize the degree of divergence existed between the healthy baseline and any current structural integrity condition since the divergence between the area of confidence ellipse of interest and the confidence circle of equivalent probability increases as the ellipse becomes thinner and more elongated, which is exactly the case where current structural integrity condition is very close to the healthy one, which, equivalently in turn, could be considered as an indicator of no damage case.

4. Description of experimental setup and procedure

Two sets of experiments were conducted as proof of concept of the previously described methodology and the introduced ECAR damage index. First of all, two cubic concrete specimens sized 150x150x150 mm (named C1, C2) were subjected to cyclic axial compressive load, with different ascending loading levels and thus damage levels, until failure. Each specimen was equipped with one PZT PIC255 attached to its surface. The concrete specimens were made by a mixing proportion of 1:0.62:2.25:3.83 (Cement: Water: Fine Aggregate: Coarse Aggregate, ratio by mean of cement). It is worth mentioning that although this test does not exactly fall in the field of damage detection, as due to the small size of the specimen there is no localization of damage. Additionally the brittle nature of the test does not allow us to observe different damage states as the increase observed in the damage indices prior to failure is connected with the increase of the

existing micro cracks that affect mainly the porosity of the specimen rather than its ability to carry loads. However this test is an excellent tool to verify the behavior of the proposed ECAR damage index compared with the RMSD damage index which is widely used for damage detection purposes. Brittle failure is abrupt so a sudden increase in the values of both damage indices is expected. The results of specimen C1 are presented in the following Figs. 6-9 and Table 1. The results of specimen C2 are presented in Table 2.

Table 1 Test information and results for specimen C1

	Load 1	Load 2	Load 3	Load 4	Load 5	Load 6	Load 7
Applied Force (kN)	173.25	339.75	418.50	497.25	576.00	639.00	679.50
Stress (MPa)	7.70	15.10	18.60	22.10	25.60	28.40	30.20
ECAR (%)	1.11	1.42	1.29	1.41	1.84	3.09	8.24
RMSD (%)	0.84	1.07	0.97	1.06	1.56	2.81	7.04
Damage	No	No	No	No	No	No	YES

Table 2 Test information and results for specimen C2

	Load 1	Load 2	Load 3	Load 4	Load 5	Load 6	Load 7
Applied Force (kN)	195.75	351.00	423.00	506.25	571.50	639.00	645.75
Stress (Mpa)	8.70	15.60	18.80	22.50	25.40	28.40	28.70
ECAR (%)	0.79	1.28	1.70	2.75	3.45	4.15	9.30
RMSD (%)	0.57	0.92	1.24	1.92	2.38	2.89	6.41
Damage	No	No	No	No	No	No	YES

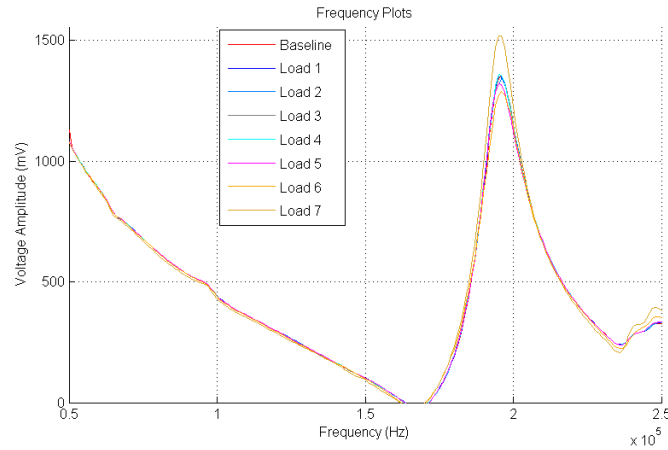Fig. 6 Concrete specimen C2 on the compression machine (Failure)

Fig. 7 Frequency Plots for load cases (Loads 1-7) (Specimen C1)
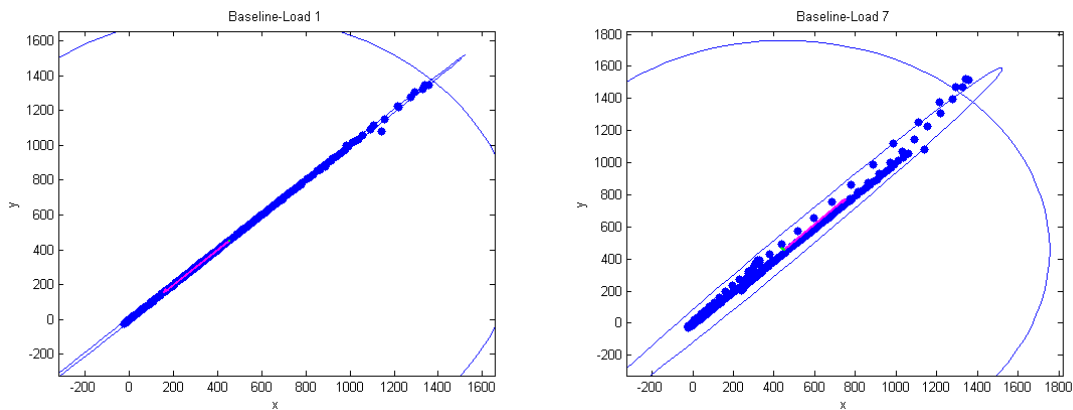

Fig. 8 Plots of confidence ellipse-circle of the damage index for Load 1 (Left) and Load 7 (Right) (Specimen C1)

In the second set of experiments four beam specimens sized 100X150X750 mm (named B1-B4) were subjected to cyclic three point bending with the same ascending load pattern as described above. Three PIC255 PZT patches were installed and three WiAMS sensing systems each connected with just one PZT were used as shown in Fig. 10. The mixing proportion was the same as the one used for the cubic specimens. The installation of the PZT patches on the surface of the concrete was done 14 days after casting of the beam specimens. The beam specimens were lightly reinforced with one rebar of structural B500C steel (Diameter 10 mm) to ensure the shear failure of the beams with minimum restriction of the widening of the bending crack which appears in the middle of the beam. The PZT actuator/sensors were bonded on the specimen surface taking into account that two of the PZT transducers (SD1 and SD2) serve as shear failure sensors while the third PZT transducer serve as bending crack sensor.

The baseline measurements were taken after placing the beam to its final position on the bending machine. Three measurements were taken in the unloaded state and their average was used as the baseline measurement of the pristine state. Afterwards, the concrete specimen was subjected to three point bending loads until failure. Measurements were taken at the end of each loading level as different damage stages exist in the structure. The first load level was for very low force in order to ensure that the tensile strength of the concrete is not exceeded and there are no cracks present yet (f_{ct} expected to be exceeded for a load of about 8 to 10 kN).
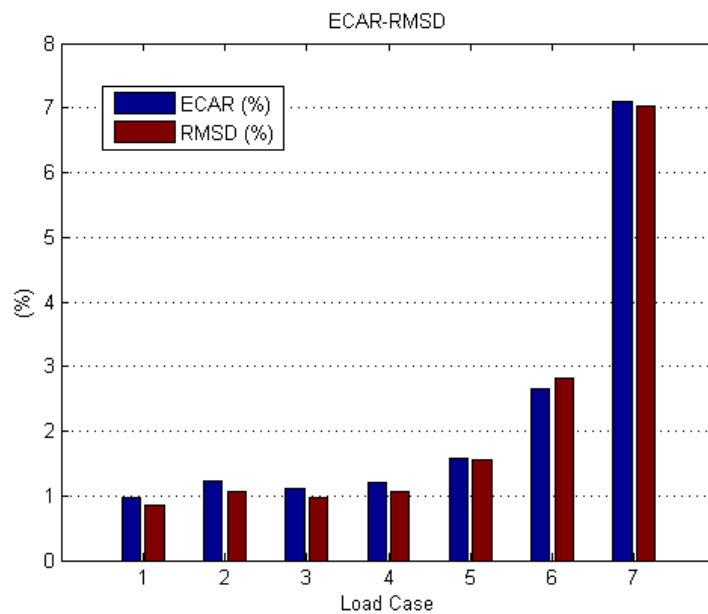
Fig. 9 RMSD and ECAR damage indices for different load cases (Specimen C1)
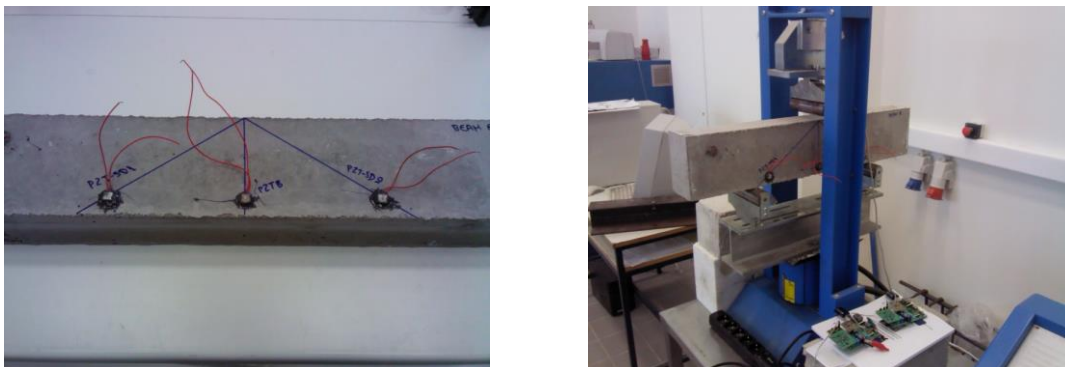

Fig. 10 Three point bending loading experimental setup and PZT locations

The results for beam specimen B1 are thoroughly presented in Table 3 and Figs. 11 to 20. The results for beam specimens B2, B3 and B4 are presented in tables 4, 5 and 6 respectively. Load cases that are titled Manual were taken after the complete failure of the beam and were manually controlled in order to widen the existing cracks. The bending crack appeared in the second load case (25.65 kN). The beam was expected to fail due to shear force which is actually the case. Failure occurred for load case 5 (57.32 kN) across the route of sensor PZT-SD1 shortly after the creation of the second shear crack. The way of failure is shown in Fig. 11.

Table 3 Test information and results for specimen B1

|		Load 1	Load 2	Load 3	Load 4	Load 5	Load 6	Load 7
	Force (kN)	8.95	25.65	36.36	55.21	57.32	Manual 1	Manual 2
PZT-B	**ECAR (%)**	0.23	0.79	0.89	1.39	1.26	1.19	2.09
	RMSD (%)	0.18	0.59	0.89	1.42	1.33	1.26	1.85
	Damage	No	YES	Yes	Yes	Yes	Yes	Yes
PZT-SD1	**ECAR (%)**	0.25	0.46	1.15	4.13	4.16	3.85	4.24
	RMSD (%)	0.20	0.37	1.43	3.49	3.52	3.23	3.60
	Damage	No	No	No	YES	Yes	Yes	Yes
PZT-SD2	**ECAR (%)**	0.15	0.34	0.60	1.50	1.68	2.38	2.15
	RMSD (%)	0.21	0.49	1.08	1.37	1.48	1.89	1.91
	Damage	No	No	No	No	YES	Yes	Yes
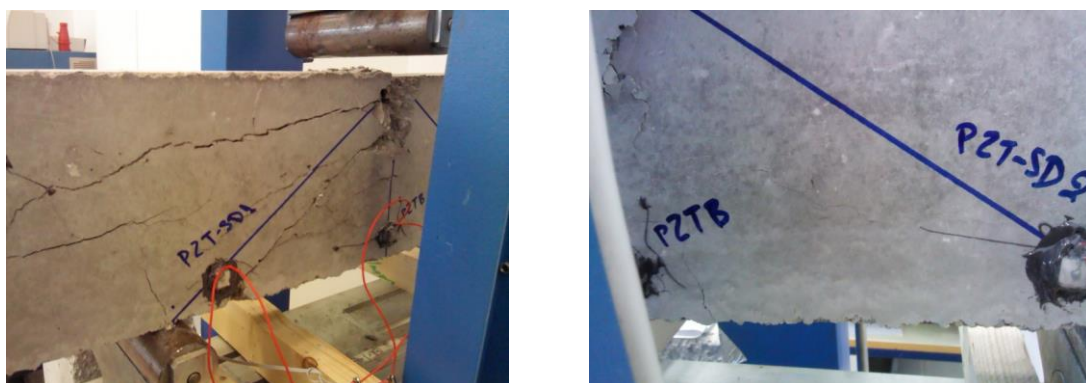
Fig. 11 Shear crack in the vicinity of PZT-SD1 (Load Case 5) and the beginning of creation of the second shear crack
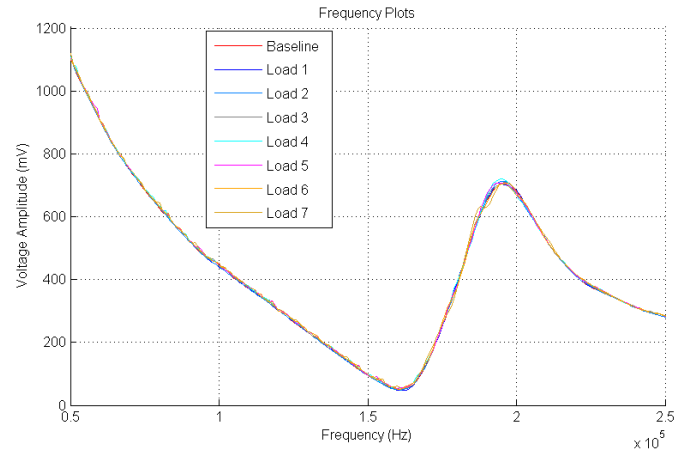
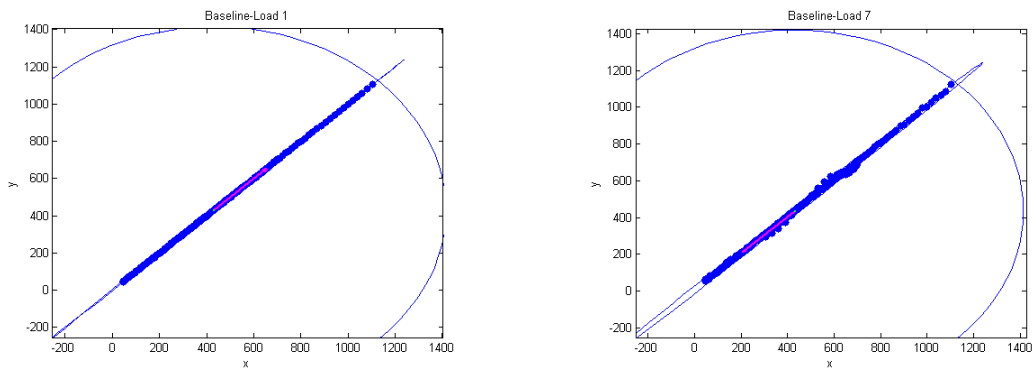Fig. 12 Peak Voltage Output spectrum plot for PZT-B transducer

Fig. 13 Plots of confidence ellipse-circle of the damage index for Load 1 (Left) and Load 7 (Right) (PZT-B)
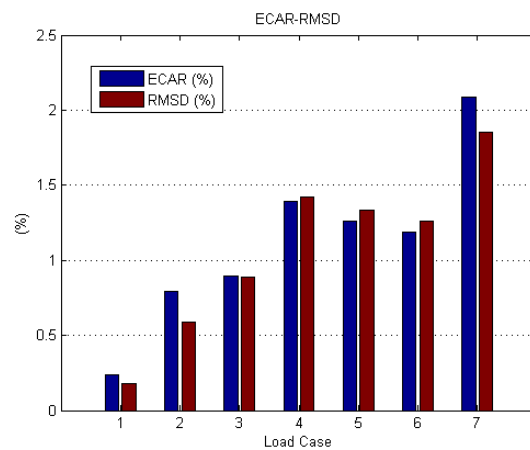

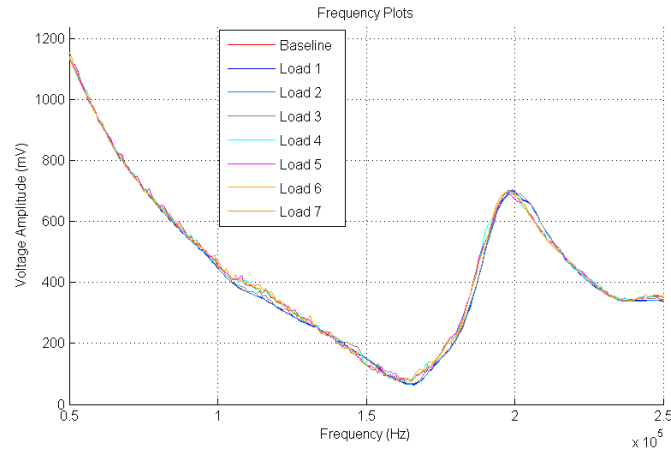Fig. 14 RMSD and ECAR damage indices for different load cases (PZT-B)

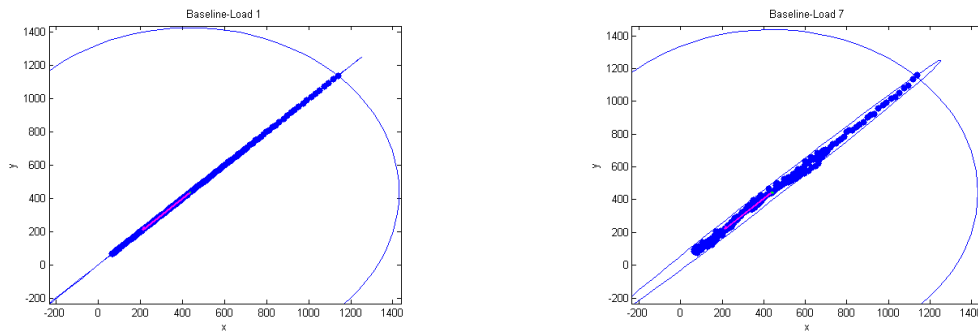Fig. 15 Peak Voltage Output spectrum plot for PZT-SD1 transducer

Fig. 16 Plots of confidence ellipse-circle of the damage index for Load 1 (Left) and Load 7 (Right) (PZT-SD1)
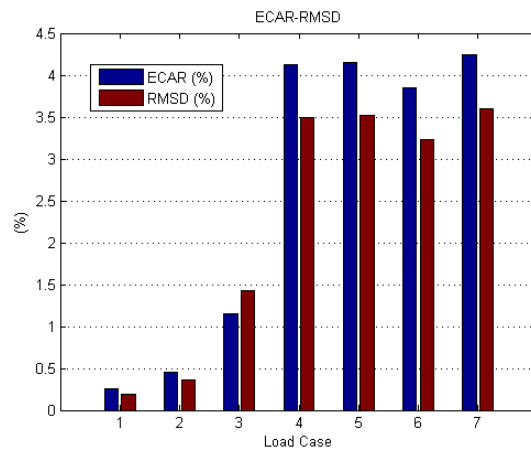

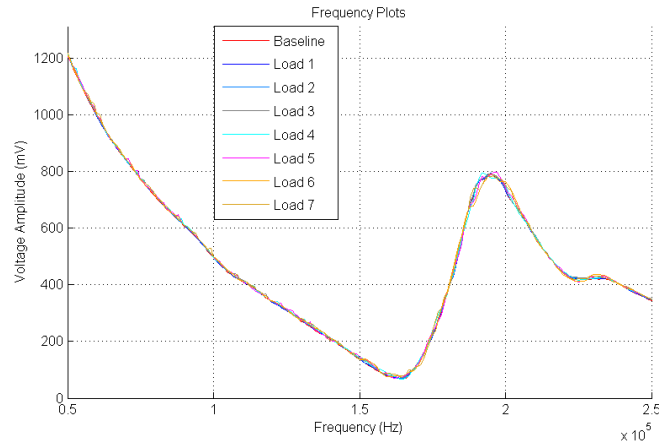Fig. 17 RMSD and ECAR damage indices for different load cases (PZT-SD1)

Fig. 18 Peak Voltage Output spectrum plot for PZT-SD2 transducer
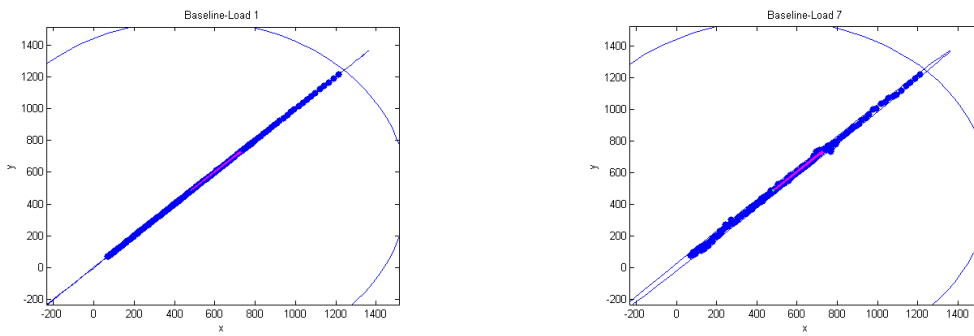

Fig. 19 Plots of confidence ellipse-circle of the damage index for Load 1 (Left) and Load 7 (Right) (PZT-SD2)
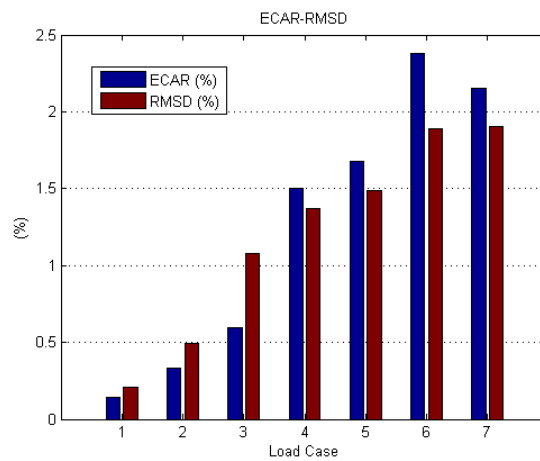

Fig. 20 RMSD and ECAR damage indices for different load cases (PZT-SD2)

The frequency plots shown in Figs. 12, 15 and 18 represent the spectrums of the detected voltage amplitude (in mV) versus frequency at the electrodes of transducers PZT-B and PZT-SD1 and PZT-SD2 respectively. The depicted results are the voltage across the PZT patch in the frequency domain, sweeping a specific range of frequencies specified by the user. In our case the sweeping range was 50-250 kHz with a frequency increment of 1 kHz. For frequencies lower than 50 kHz changes in the structural integrity of the structure will be "drowned" by the capacitive nature of the PZT in that specific bandwidth, and for frequencies higher than 250 kHz the PZT patch is more sensitive in changes of its own conditions rather than changes in the structure. Therefore, changes in the peak output voltage measured across the PZT electrodes result in changes between the pristine state and the damaged state which will be used as alarm for damage detection. As far as ECAR (Ellipse-to-Circle-Area-Ratio) damage index is concerned, Figs. 13, 16 and 19 are the visual outcomes of what is described in previous chapter 3. The axes shown in those figures are peak output voltage for the baseline state vs. peak output voltage for any current loading state and what is graphically shown are the error ellipse and the error circle for a probability or confidence level of 99.5%. The images are for baseline measurement and load case 1 (left image, low damage i.e., ellipse degenerates to line) and baseline measurement and load case 7 (right image, damaged state). The ratio of the area of the error ellipse to the area of the error circle is used as the ECAR damage index (Figs. 14, 17 and 20).

The results of the rest of the specimens are similar to the ones presented for B1. It is worth mentioning that in specimen B3 the bending crack is not detected due to faulty PZT. Another point that needs to be pointed out is big value of the damage indices in specimen B4 for the sensor PZT-B. In the particular specimen, the bending crack passed directly through the PZT sensor resulting in the detachment of part of the epoxy used to attach the sensor on the beam. The difference is also obvious observing the frequency plots (Fig. 21).

Table 4 Test information and results for specimen B2

		Load 1	Load 2	Load 3	Load 4	Load 5	Load 6	Load 7	Load 8	Load 9	Load 10
	Force (kN)	7.28	15.35	20.81	25.01	30.16	35.32	39.34	40.30	Manual	Manual 2
PZT-B	ECAR (%)	0.58	1.56	1.82	2.20	2.23	2.11	1.94	1.70	1.52	1.35
	RMSD (%)	0.59	1.59	1.83	2.20	2.21	2.09	1.85	1.61	1.43	1.26
	Damage	No	YES	Yes	Yes	Yes	Yes	Yes	Yes	Yes	Yes
PZT-SD1	ECAR (%)	0.21	0.39	0.50	0.55	0.66	0.76	0.86	0.91	0.90	0.90
	RMSD (%)	0.17	0.31	0.39	0.44	0.53	0.61	0.69	0.74	0.74	0.74
	Damage	No	No	No	No	No	No	No	No	No	No
PZT-SD2	ECAR (%)	0.22	0.38	0.46	0.54	0.63	0.72	1.62	3.84	2.84	4.86
	RMSD (%)	0.16	0.28	0.34	0.39	0.47	0.54	1.20	2.95	2.24	3.74
	Damage	No	No	No	No	No	YES	Yes	Yes	Yes	Yes

Table 5 Test information and results for specimen B3

		Load 1	Load 2	Load 3	Load 4	Load 5	Load 6	Load 7	Load 8
	Force (kN)	8.19	16.20	22.90	27.77	33.08	38.07	41.20	Manual
PZT-B	**ECAR (%)**	0.21	0.77	0.83	0.90	0.93	1.02	1.10	1.10
	RMSD (%)	0.21	0.76	0.81	0.88	0.91	1.00	1.08	1.08
	Damage	No	YES	Yes	Yes	Yes	Yes	Yes	Yes
PZT-SD1	**ECAR (%)**	0.84	1.10	1.22	1.70	2.54	2.21	2.60	2.63
	RMSD (%)	0.96	1.20	1.28	1.61	2.22	1.93	2.16	2.17
	Damage	No	No	No	No	No	YES	Yes	Yes
		Load 1	Load 2	Load 3	Load 4	Load 5	Load 6	Load 7	Load 8
PZT-SD2	**ECAR (%)**	1.18	1.41	2.01	4.33	4.49	4.52	3.95	3.86
	RMSD (%)	0.89	1.05	1.51	3.22	3.33	3.37	2.95	2.88
	Damage	No	No	No	YES	Yes	Yes	Yes	Yes

Table 6 Test information and results for specimen B4

|		Load 1	Load 2	Load 3	Load 4	Load 5	Load 6	Load 7	Load 8
	Force (kN)	7.28	17.72	25.14	30.08	35.55	40.43	41.79	Manual
PZT-B	**ECAR (%)**	3.18	22.01	23.80	23.97	24.33	24.69	24.37	25.49
	RMSD (%)	2.26	16.90	18.12	18.21	18.45	18.69	18.48	19.25
	Damage	No	YES	Yes	Yes	Yes	Yes	Yes	Yes
PZT-SD1	**ECAR (%)**	0.40	0.96	3.51	3.40	3.44	4.37	4.71	7.33
	RMSD (%)	0.33	0.77	2.93	2.80	2.86	3.58	4.22	6.59
	Damage	No	No	No	YES	Yes	Yes	Yes	Yes
PZT-SD2	**ECAR (%)**	0.51	0.98	1.34	1.47	1.73	1.86	2.66	2.77
	RMSD (%)	0.40	0.77	1.04	1.16	1.36	1.47	2.07	2.16
	Damage	No	No	No	No	No	YES	Yes	Yes
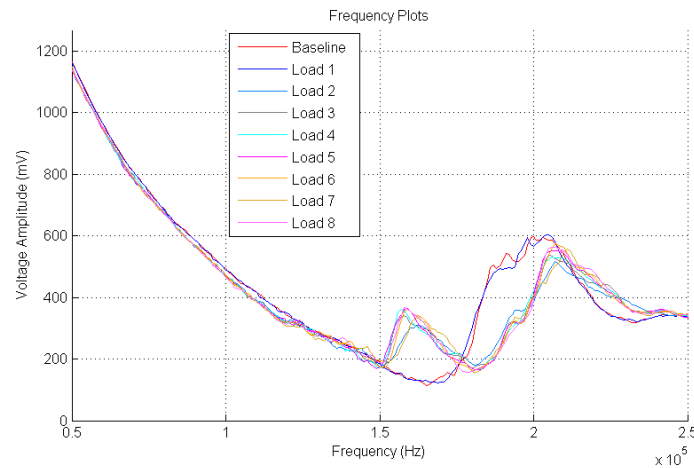
Fig. 21 Peak Voltage Output spectrum plot for PZT-B transducer of B4

5. Conclusions

This paper presents an innovative wireless structural health monitoring system based on an alternative version of electromechanical impedance (admittance) technique. The feasibility of the proposed WiAMS has been investigated by using a new damage identification index based on the implementation of statistical error regions as being the error ellipse and the error circle under specific probability. The WiAMS was successfully applied to laboratory experiments on concrete beam specimens. The proposed monitoring system was able to successfully correlate peak output voltage response signals to the onset of damage while in the same time its performance depends on the specific characteristics of its components. The results demonstrated that WiAMS gives the benefit of damage detection in early stages of concrete structures.

Acknowledgements

References

Annamdas, V.G.M., Yang, Y. and Soh, C.K. (2010), "Impedance based concrete monitoring using embedded PZT sensors", *Int. J. Civil Struct. Eng.*, **1**(3), 414-424.
Chin, G.Y. (1987), *Two Dimensional Measures Of Accuracy In Navigational Systems*, Technical Report

DOT-TSC-RSPA-87-1. US Dept of Transportation.

Mertikas, S. (1994), *Error Distributions And Accuracy Measures In Navigation : An Overview*, Technical Report No.113, Dept. Surveying Engng., Univ of New Brunswick, Canada.

Na, S. and Lee, H.K. (2012), "A technique for improving the damage detection ability of the electro-mechanical impedance method on concrete structures", *Smart Mater. Struct.*, **21**(8), 085024:1–085024:9.

Park, G., Cudney, H.H. and Inman, D.J. (2000), "Impedance-based health monitoring of civil structural components", *Infrastuct. Syst.*, **6**(4), 153-160.

Park, G., Cudney, H.H. and Inman, D.J. (2000), "Overview of piezoelectric impedance-based health monitoring and path forward", *Shock Vib. Dig.*, **35**(6), 451-463.

Park, S., Ahmad, S., Yun, C.B. and Roh, Y. (2006), "Multiple crack detection of concrete structures using impedance-based structural health monitoring techniques", *Exp. Mech.*, **46**(5), 609-618.

Park, S., Kim, J.W., Lee, C. *et al*. (2011), "Impedance-based wireless debonding condition monitoring of CFRP laminated concrete structures", *NDT & E Int.*, **44**(2), 232-238.

Peairs, D.M., Park, G. and Inman, D.J. (2004), "Improving accessibility of the impedance-based structural health monitoring method", *J. Intel. Mat. Syst. Str.*, **15**(2), 129-139.

Providakis, C.P., Tsistrakis, S., Voutetaki, M., Tsompanakis, J., Stavroulaki, M., Agadakos, J., Kampianakis, L. and Pentes, G. (2015), "WiAMS: An innovative wireless damage detection monitoring system using electromechanical impedance-based and extreme value statistical approach", *J. Struct. Control Health Moni.*, submitted.

Sekhar, A.S. (2008), "Multiple cracks effect and identification", *Mech. Syst. Signal Pr.*, **22**(4), 845-878.

Shin, S.W. and Oh, T.K. (2009), "Application of electro-mechanical impedance sensing technique for online monitoring of strength development in concrete using smart PZT patches", *Construct. Build. Mater.*, **23**(2), 1185-1188.

Song, G., Gu, H., Mo, Y.L., Hsu, T. and Dhonde, H. (2007), "Concrete structural health monitoring using embedded piezoceramic transducers", *Smart Mater. Struct.*, **16**(4), 959-968.

Tawie, R. and Lee, H.K. (2010), "Monitoring the strength development in concrete using EMI sensing technique", *Construct. Build. Mater.*, **24**(9), 1746-1753.

Tawie, R. and Lee, H.K. (2011), "Characterization of cement based materials using a reusable piezoelectric impedance based sensor", *Smart Mater. Struct.*, **20**(8), 085023.

Tseng, K.K. and Wang, L. (2004), "Smart piezoelectric transducers for in situ health monitoring of concrete", *Smart Mater. Struct.*, **13**(5), 1017-1024.

Tseng, K.K.H., Soh, C.K. and Naidu, A.S.K. (2001), "Non-parametric damage detection and characterization using smart piezoelectric material", *Smart Mater. Struct.*, **11**(3), 317-329.

Wang, D.S. and Zhu, H.P. (2011), "Monitoring of the strength gain of concrete using embedded PZT impedance transducer", *Constr. Build. Mater*., **25**(9), 3703-3708.

Yang, Y. and Divsholi, B.S. (2010), "Sub-frequency interval approach in electromechanical impedance technique for concrete structure health monitoring", *Sensors*, **10**(12), 11644-11661.

Yang, Y., Hu, Y. and Lu, Y. (2008), "Sensitivity of PZT impedance sensors for damage detection of concrete structures", *Sensors*, **8**(1), 327-346.